Vietnam Journal of Science and Technology ***63*** *(5) (2025) 960-971*

doi:10.15625/2525-2518/18571

Numerical simulation and experimental study on effect of cooling rate on microstructure and strength of nanostructured materials

Nguyen Hong Hai[1], Le Minh Duc[2], Hoang Thi Ngoc Quyen[1], Pham Quang[1, *]

[1]*Faculty of Materials Engineering, School of Materials Science and Engineering, Hanoi University of Science and Technology, No. 1 Dai Co Viet, Ha Noi, Viet Nam*

[2]*Department of Materials Science and Engineering, Faculty of Mechanical Engineering, Le Quy Don Technical University, No. 236 Hoang Quoc Viet, Ha Noi, Viet Nam*

[*]Email: *quang.pham@hust.edu.vn*

Received: 23 July 2023; Accepted for publication: 15 April 2024

Abstract. This study examines the effect of cooling rate on the microstructure and mechanical properties of Al-based two-phase nanostructured materials cast through a copper mold. Using both numerical simulation via the finite element method (FEM) and experimental analysis, product thicknesses from 0.3 to 20 mm were investigated. The simulated cooling rates ranged from approximately 10^2 to 10^4 K/s, showing that the size of intermetallic precipitates decreased with increasing cooling rate. The Abaqus/Standard platform was used for uncoupled heat transfer analysis, accounting for temperature-dependent conductivity, latent heat, and boundary conditions involving convection and radiation. Automatic time stepping was applied for numerical stability, and first-order heat transfer elements effectively captured latent thermal effects. The results demonstrate that optimizing the cooling rate refines the microstructure and enhances the alloy's strength, confirming the effectiveness of combined experimental and simulation approaches in improving casting process design.

Keywords: Aluminium based, Al–Mn series, nanostructured, metallic glass, cooling rate, solidification, FEM simulation, Abaqus/Standard, uncoupled heat transfer analysis.

Classification numbers: 2.9.1, 4.10.4, 5.9.3.

1. INTRODUCTION

Quasicrystals are generally classified into aluminium-, magnesium-, and titanium-based systems, among which aluminium-based alloys have been most extensively investigated due to their low cost, wide availability, and non-toxic nature. Within this category, the Al–Cu–Fe and Al–Mn systems have attracted significant attention. In particular, Al–Mn alloys are widely used because they allow partial formation of the pure aluminium phase, thereby improving ductility and reducing brittleness compared with other quasicrystalline alloys [1 - 3].

Rheo-die casting technology, which combines the advantages of rheocasting and die casting, enables the formation of a semi-solid slurry and laminar metal flow. Unlike conventional high-pressure die casting, where turbulent flow can entrap gas and create porosity, rheo-die casting provides smoother mold filling and a more uniform microstructure due to lower pouring temperatures, typically between the liquidus and solidus ranges [4–8]. Recent studies by the authors' research group have focused on producing semi-solid Al–Mn alloys with a globular α-phase structure through continuous rheocasting and rheo-die casting routes.

For Al-based cast alloys, the cooling rate plays a decisive role in microstructural evolution. Increasing the cooling rate refines α-Al grains and suppresses the growth of secondary phases, leading to enhanced strength and overall mechanical performance [9 - 12]. However, Al–Mn alloys exhibit relatively poor thermal stability because of their sub-stable microstructure. To address this, various transition-group elements such as Fe, Be, and Ce have been introduced to stabilize the structure and promote the formation of the icosahedral (I-) phase [13 - 17]. While beryllium additions enhance I-phase nucleation, their severe toxicity limits practical use [18 - 21]. Cerium has been proposed as a promising alternative to improve I-phase formation under diverse solidification conditions, although its effectiveness remains a subject of ongoing debate among researchers [22, 23].

Combined with related studies [24 - 27], the addition of Fe not only increases the thermal stability of the alloy but also increases the ability to form quasicrystalline phases, and Fe is cheap, readily available, and non-toxic. The effect of iron addition on the formed phases of the alloy has also been studied in the literature [28], but there are few systematic studies on the types, morphology, and thermal expansion properties of alloy phases formed in different preparation processes.

In this study, by numerical simulation (ABAQUS, FEM) [29] and experimental methods, the cooling rate was investigated by changing the product thickness (0.3, 0.5, 1, 2, 3 and 20 mm) of Al based two-phase nanostructured materials casted through a copper mold. The simulation and experimental results show that the precipitated intermetallic phases have a decreasing size corresponding to the increasing cooling rates.

2. METHODOLOGY AND MODELING

The Abaqus/Standard module for uncoupled heat transfer analysis simulates solid-body heat conduction with temperature-dependent conductivity, internal energy including latent heat, and generalized convection and radiation boundary conditions. This work employs its fundamental framework encompassing energy balance, constitutive modeling, boundary definitions, finite element discretization, and time-integration algorithms [30].

2.1. The basic energy balance (Green and Naghdi)

$$\int_V \boldsymbol{\rho \dot{U} dV} = \int_S \boldsymbol{q dS} + \int_V \boldsymbol{r dV} \tag{1}$$

where V is a volume of solid material, with surface area S; $\boldsymbol{\rho}$ is the density of the material; $\boldsymbol{\dot{U}}$ is the material time rate of the internal energy; q is the heat flux per unit area of the body, flowing into the body; and r is the heat supplied externally into the body per unit volume.

It is assumed that the thermal and mechanical problems are uncoupled in the sense that $\boldsymbol{U = U(T)}$ only, where $\boldsymbol{T}$ is the temperature of the material, and q and r do not depend on the strains or displacements of the body. For simplicity a Lagrangian description is assumed, so "volume" and "surface" mean the volume and surface in the reference configuration.

2.2. Specific heat, latent heat

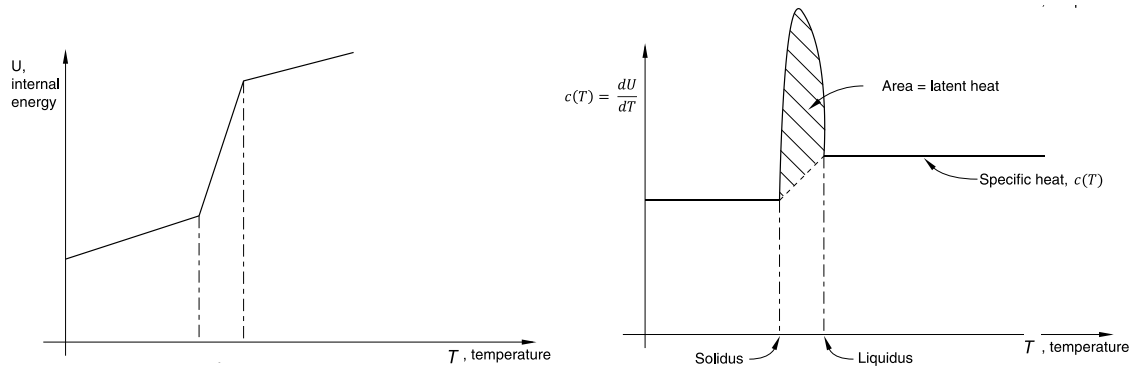

Figure 1. Specific heat, latent heat definition [30].

The temperature dependence of internal energy is expressed through the specific heat::

$$\boldsymbol{c(T) = \frac{dU}{dT}} \tag{2}$$

Latent heat effects accompanying phase transformation are defined by the solidus and liquidus temperatures and the total internal energy change associated with the transition. This contribution is added to the sensible heat (Figure 1). The phase change is typically assumed to occur within a prescribed temperature range, although kinetic modeling may be required for improved accuracy.

Heat conduction follows Fourier's law:

$$\boldsymbol{f = -k\frac{\partial T}{\partial x}} \tag{3}$$

where $k = k(T)$is the conductivity matrix; f is the heat flux; and x is position. The conductivity k can be fully anisotropic, orthotropic, or isotropic.

2.3. Boundary conditions

Boundary conditions can be specified as prescribed temperature $\boldsymbol{T = T(x,t)}$; prescribed surface heat flux, $\boldsymbol{q = q(x,t)}$ per area; prescribed volumetric heat flux $\boldsymbol{q = r(x,t)}$ per volume; surface convection: $\boldsymbol{q = h(T - T^0)}$, where $\boldsymbol{h = h(x,t)}$ is the film coefficient and $\boldsymbol{T^0 = T^0(x,t)}$ is the sink temperature; and radiation: $\boldsymbol{q = A(T - T^Z)^4 - (T^0 - T^Z)^4}$, where A is the radiation constant (emissivity times the Stefan-Boltzmann constant) and $\boldsymbol{T^Z}$ is the value of absolute zero on the temperature scale being used.

2.4. Spatial discretization

A variational statement of the energy balance, Equation 1, together with the Fourier law, Equation 3, is obtained directly by the standard Galerkin approach as

$$\boldsymbol{\int_V \rho \dot{U} \delta T dV + \int_V \frac{\partial \delta T}{\partial x} k \frac{\partial T}{\partial x} dV = \int_V \delta T r dV + \int_{S_q} \delta T q dS} \tag{3}$$

where $\boldsymbol{\delta T}$ is an arbitrary variational field satisfying the essential boundary conditions. The body is approximated geometrically with finite elements, so the temperature is interpolated as

$$\boldsymbol{T = N^N(x)T^N, N = 1, 2, ...}$$

where $\boldsymbol{T^N}$ are nodal temperatures. The Galerkin approach assumes that the variational field is interpolated by the same functions:

$$\boldsymbol{\delta T = N^N \delta T^N}$$

with these interpolations, the variational statement (used $\boldsymbol{N^N}$) and since the $\boldsymbol{\delta T^N}$ are arbitrarily chosen, this gives the system of equations:

$$\boldsymbol{\int_V N^N \rho U \dot{d}V + \int_V \frac{\partial N^N}{\partial x} k \frac{\partial T}{\partial x} dV = \int_V N^N r dV + \int_{S_q} N^N q dS} \quad (4)$$

2.5. Time integration

Abaqus/Standard uses the backward difference algorithm:

$\boldsymbol{\dot{U}_{t+\Delta t} = (U_{t+\Delta t} - U_t)\left(\frac{1}{\Delta t}\right)}$(5)

This operator is chosen for a number of reasons. First of all, we choose from one-step operators of the form:

$$\boldsymbol{f_{t+\Delta t} = f_t + ((1-\gamma)\dot{f}_t + \gamma \dot{f}_{t+\Delta t})\Delta t}$$

However, that form of the operator tends to produce oscillations in the early-time solution that are not present in the backward difference form. Thus, we use $\boldsymbol{\gamma = 1}$: backward difference. Introducing the operator, Equation 5, into the energy balance Equation 4 gives:

$$\boldsymbol{\frac{1}{\Delta t}\int_V N^N \rho\,(U_{t+\Delta t} - U_t) dV + \int_V \frac{\partial N^N}{\partial x} k \frac{\partial T}{\partial x} dV - \int_V N^N r dV - \int_{S_q} q dS = 0} \quad (6)$$

This nonlinear system is solved by a modified Newton method. The formation of the terms in this tangent matrix is now described.

The internal energy term gives a Jacobian contribution:

$$\boldsymbol{\frac{1}{\Delta t}\int_V N^N \rho \left.\frac{dU}{dT}\right|_{t+\Delta t} N^M dV}$$

$\boldsymbol{(dU/dT)|_{t+\Delta t}}$: is the specific heat, $\boldsymbol{c(T)}$, outside the latent heat range, and is $\boldsymbol{c + L/(T_L - T_S)}$ if $\boldsymbol{T_L > T_{t+\Delta t} > T_S}$ at the integration point, where $\boldsymbol{T_L}$ and $\boldsymbol{T_S}$ are the liquidus and solidus temperatures and *L* is the latent heat associated with this phase change.

With film and radiation conditions, the surface flux term gives a Jacobian contribution:

$$\boldsymbol{\int_S N^N \frac{\partial q}{\partial T}|_{t+\Delta t} N^M dS}$$

For film conditions, $\boldsymbol{q = h(T)(T - T^0)}$, $\boldsymbol{\frac{\partial q}{\partial T} = \frac{\partial h}{\partial T}\left(T - T^0\right) + h}$

while for radiation, $\boldsymbol{q = A\left(T^4 - T^{0\,4}\right)}$, $\boldsymbol{\frac{\partial q}{\partial T} = 4AT^3}$

These terms are included in exactly this form in the Jacobian. The modified Newton method is then:

$$\boldsymbol{\left[\frac{1}{\Delta t}\int_V N^N \rho \left.\frac{dU}{dT}\right|_{t+\Delta t} N^M dV + \int_V \frac{\partial N^N}{\partial x} k|_{t+\Delta t} \frac{\partial N^M}{\partial x} dV + \int_S N^N \left(\frac{\partial h}{\partial T}\left(T - T^0\right) + h + 4AT^3\right) N^M \partial S\right] c^{-M} = \int_V N^N r dV + \int_S N^N q dS - \frac{1}{\Delta t}\int_V N^N \rho (U_{t+\Delta t} - U_t) dV - \int_V \frac{\partial N^N}{\partial x} k \frac{\partial T}{\partial x} dV}$$

with $\boldsymbol{T^N_{t+\Delta t, i+1} = T^N_{t+\Delta t, i} + c^{-N},\ i = iteration\ number}$ (7)

For purely linear systems, Equation 7 is linear in $\boldsymbol{c^{-M}}$ and, hence, in $\boldsymbol{T^{N}_{t+\Delta t}}$, so a single equation solution provides the $\boldsymbol{T^{N}_{t+\Delta t}}$. Since the method is usually only a minor modification of Newton's method, convergence is rapid.

3. MODELING AND EXPERIMENTAL

2.1. Modeling and Simulation

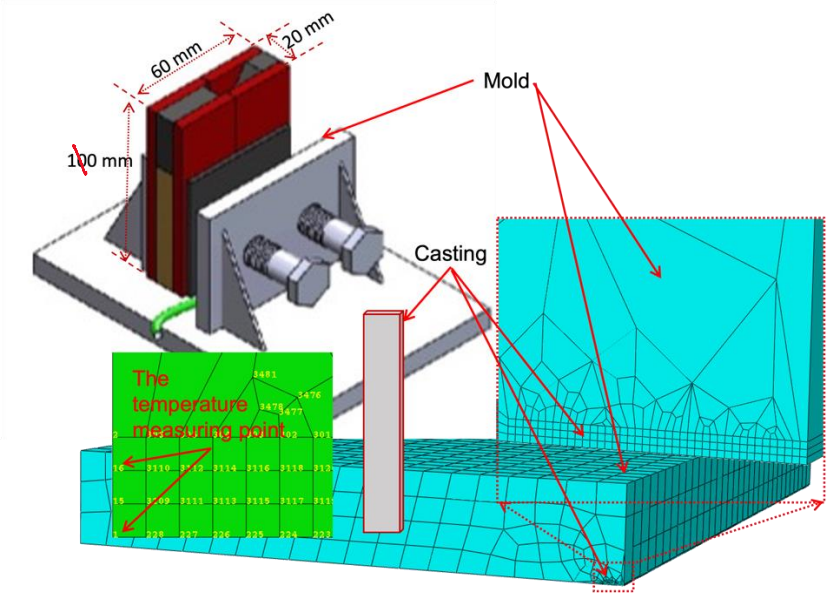

Figure 2. Casting mold system used in experiments and simulations.

Table 1. Thermo-physical properties [31].

Thermo-physical property	AlMnCe		Mold (Cu)
	Solid	Liquid	
Temperature (^oC)	705	730	25
Bulk density (kg/m^3)	2720	2385	8940
Specific heat capacity ($J/kg.K$)	904	108	380
Thermal conductivity ($W/m.K$)	226	105	380
Latent heat (J/kg)		360000	

The casting mold system used in experiments and simulations is shown in Figure 2. The mold is made of pure copper material, smoothed flat and polished on all sides, the dimensions are 60 mm in width, 110 mm in height, and 20 mm in thickness. A vacuum system is designed to prevent oxidation and speed up the mold filling of the casting. The castings had a height of 100 mm, with different thicknesses: 0.3, 0.5, 1, 2, 3 and 20 mm.

By using 3D simulation, the developed model calculated and simulated processes with a combination of heat exchange and solid-liquid phase transition. Figure 2 shows the modeling and meshing in the calculation with total node numbers of 11220, 9512, 8036, 7052, 7093 for

9450, 7840, 6480, 5600, 5640 heat transfer elements, respectively. The steady conduction solution for this problem was computed.

The initial temperature of the liquid AlMnCe alloy was 1000 ^{o}C. The contact between the mold and the melt was selected as the film conditions. Data for the thermo-physical properties are presented in Table 1.

2.3. Experimental (Microstructure characterization and tensile testing)

In this study, raw AlMnCe materials were used. The samples were dosed according to the atomic ratio of $Al_{92}Mn_6Ce_2$ (in atomic percent, at%) and melted in an intermediate frequency induction melting furnace. The mold was designed similarly to the one in the simulation problem. The castings with a height of 100 mm and different thicknesses (0.5, 1, 2, 3 and 20 mm) were fabricated to achieve different cooling rates and to investigate the effect of the cooling rate on the microstructure and mechanical properties.

The polished casting specimens were observed using a HITACHI S-4800 field-emission scanning electron microscope (SEM) equipped with an X'pert Pro of Malvern Panalytical energy dispersive spectroscope (EDS, EDX) and Digital optical microscopy (VHX-7000).

Moreover, tensile tests were performed on an INSTRON 3382 tensile machine at room temperature using sheet specimens.

3. RESULTS AND DISCUSSION

The temperature data were numerically calculated at casting sites with different thicknesses, as shown in Table 2.

Table 2. Temperature data calculated at casting sites with different thicknesses.

Time	Near surface						Center					
	03 mm	**0.5 mm**	**1 mm**	**2 mm**	**3 mm**	**20 mm**	**03 mm**	**0.5 mm**	**1 mm**	**2 mm**	**3 mm**	**20 mm**
0	1000	1000	1000	1000	1000	1000	1000	1000	1000	1000	1000	1000
0.1	45.474	58.261	91.996	151.887	198.612	550.136	46.397	59.490	96.333	165.930	241.781	828.819
0.2	31.815	34.734	43.864	61.041	82.404	487.417	31.793	34.732	43.971	61.959	87.098	748.524
0.3	28.740	30.357	35.360	44.412	56.734	470.789	28.734	30.355	35.371	44.541	57.583	730.799
0.4	27.654	28.848	32.459	38.903	47.835	460.371	27.652	28.847	32.463	38.945	48.129	729.893
0.5	27.146	28.135	31.087	36.335	43.672	452.779	27.145	28.134	31.089	36.356	43.824	729.369
0.6	26.858	27.725	30.298	34.865	41.292	447.161	26.858	27.725	30.299	34.879	41.389	727.735
0.7	26.672	27.457	29.779	33.901	39.728	442.976	26.672	27.457	29.780	33.910	39.799	724.166
0.8	26.540	27.263	29.404	33.204	38.595	439.184	26.540	27.263	29.404	33.211	38.650	716.441
0.9	26.438	27.113	29.114	32.665	37.716	434.742	26.438	27.113	29.114	32.672	37.760	685.240
1	26.356	26.992	28.879	32.229	37.001	427.639	26.356	26.992	28.879	32.234	37.037	616.894

Figure 3 represents the temperature profile numerically calculated at casting sites with different thicknesses varying from 0.3 to 20 mm in the cooling channel. The largest cooling rate is found to be about ~10^4 K/s at the casting sites with thicknesses of 0.3, 0.5 and 1 mm. With the other thinknesses of 2 and 3 mm, the cooling is slower, with a reduced cooling rate of 10^3 K/s (at

the center of the casting) and ~ 10^4 K/s (at the surface of the casting). In the case of a 20 mm thick casting, the cooling rate at the surface is ~ 10^3 K/s, while at the center of the casting, the cooling rate is the same as that in conventional die casting (~ 10^2 K/s). In particular, the cold line shows the heat retention capacity, demonstrating the role of latent heat in the solidification process.

As we know, extremely cool liquid metals will turn into an amorphous state when the crystallization process is hindered. Amorphous materials obtained at different cooling rates will have different structures. However, because aluminium is difficult to become amorphous with low GFA (glass forming ability), cooling speeds of about 10^4 K/s (casting in vacuum copper die, 0.3 and 0. 5 mm) are still not enough to create an amorphous state.

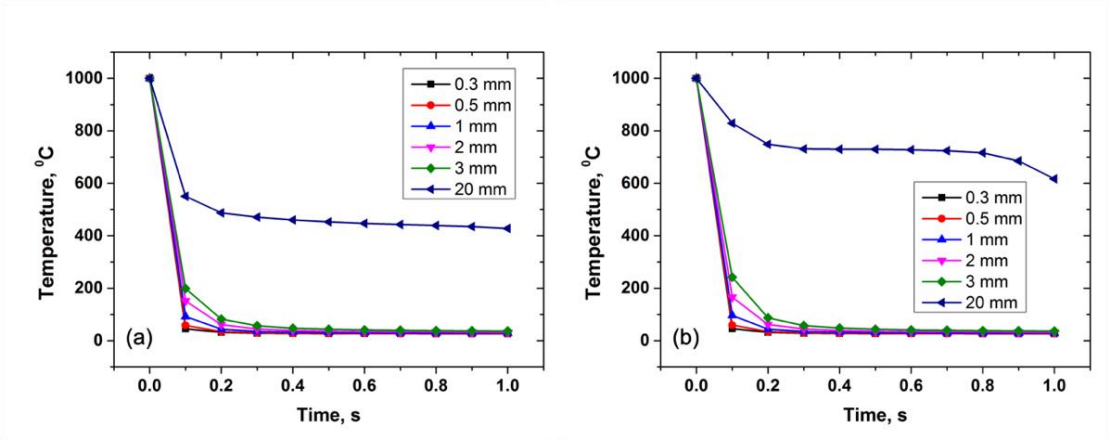

Figure 3. Temperature profile results (a) at near surface and (b) at the center of the casting.

Figure 4 shows the cooling rate curves at the near surface between the casting and the center of the as-cast alloys during solidification. We see that the cooling rate is not significantly different with casting thicknesses of 0.3, 0.5, 1 mm, less with thicknesses of 2, 3 mm and large with a thickness of 20 mm.

The effect of cooling speed with different thicknesses of 20, 3, 1 and 0.5 mm corresponds to increasing cooling rates of 10^2, 10^3 and 10^4 K/s, respectively. It can be clearly seen that the secreted intermetallic phases have a decreasing size: when the cooling speed is 10^2 K/s (Figure 7), the intermetallic phase has a rather coarse size (10 - 20 μm) due to its long contact time with liquid metal and favorable conditions for growth. At such a low cooling rate, a phase with a high atomic number, $Al_{18}Mn_4Ce_2$ also known as the "τ" phase) can be formed instead of $Al_{20}Mn_2Ce_2$ since the Mn and Ce atoms diffuse into this phase.

When adding alloy elements to aluminium (in liquid state), it often creates an Al-alloy element phase diagram (Figure 5). The alloying element can dissolve in Al to form a solid solution, or, when it exceeds the solubility limit (DF line), it will create a second phase. Based on the transformation temperature, the inflection points correspond to the formations of α-Al dendrite and eutectic phases, respectively. It is evident that the formation of α-Al occurs first, at the beginning of solidification, while the formation of eutectic phase comes later and the solidification happens at the end.

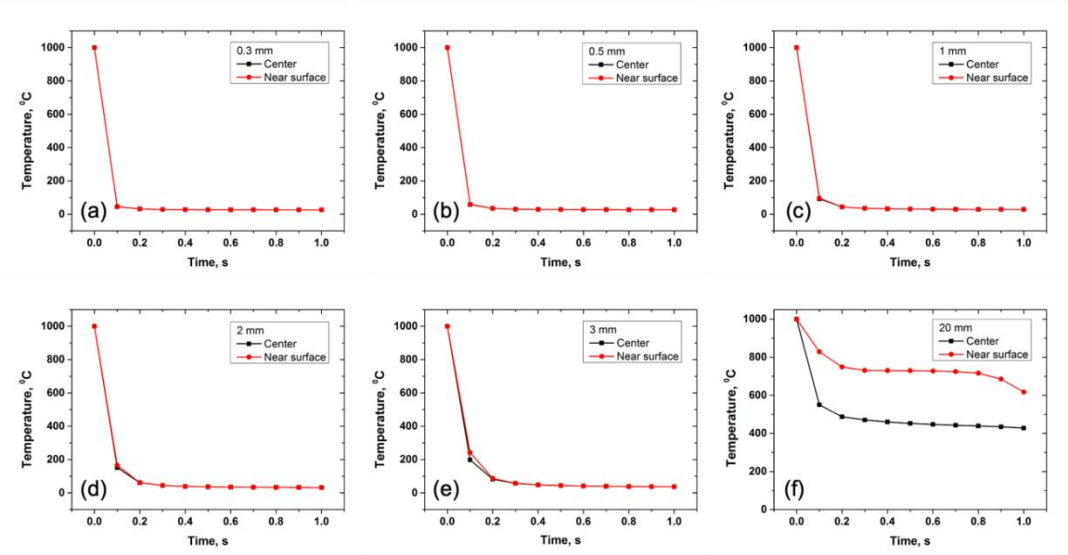

Figure 4. Temperature profile results at near surface and the center for thicknesses of 0.3 mm (a), 0.5 mm (b), 1 mm (c), 2 mm (d), 3 mm (e), and 20 mm (f) of the casting.

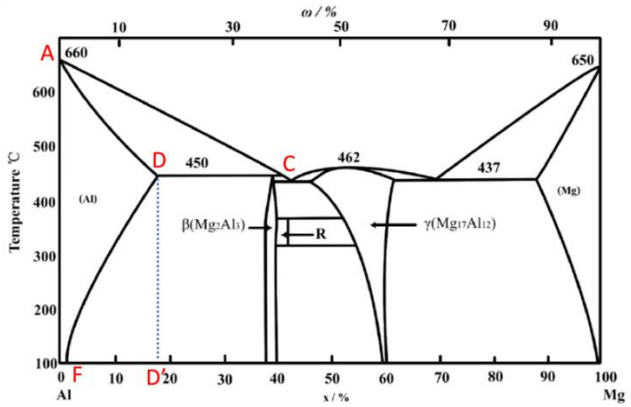

Figure 5. Phase diagram of Al-Mn alloys [31].

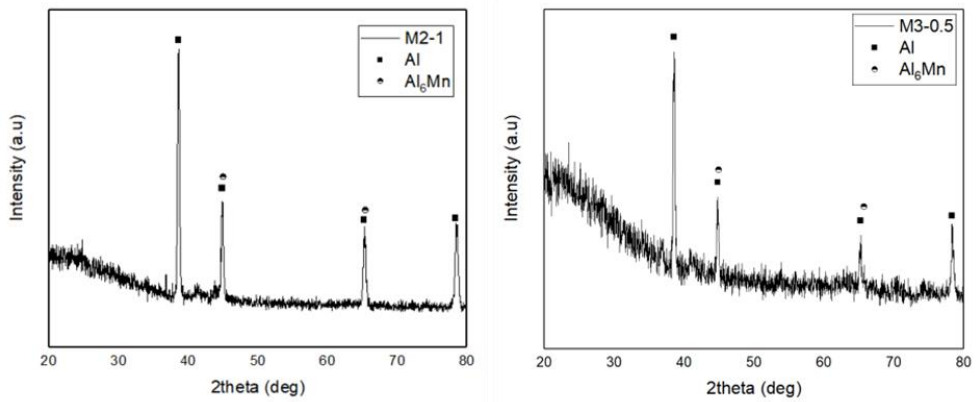

Figure 6. Analysis of X-ray diffraction thicknesses: 1 mm (M2-1) and 0.5 mm (M3-0.5).

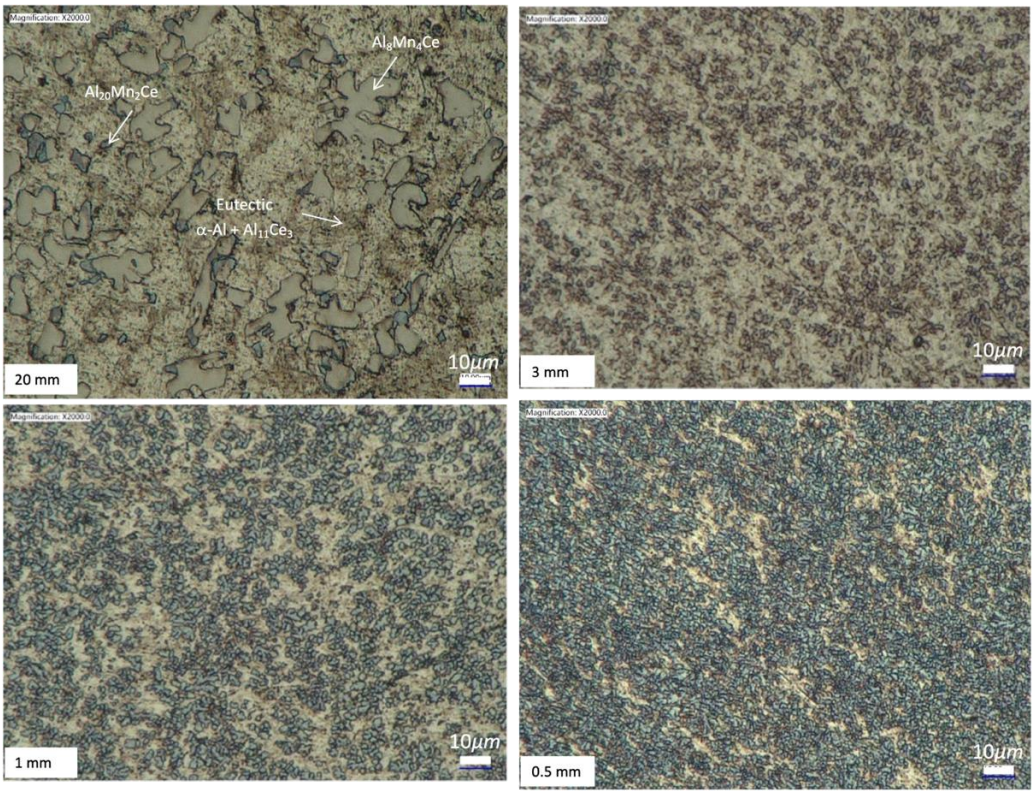

Figure 7. Microscopic organization with different thicknesses (20, 3, 1, 0.5 mm), corresponding to the cooling rates of 10^2, 10^3, and 10^4 K/s.

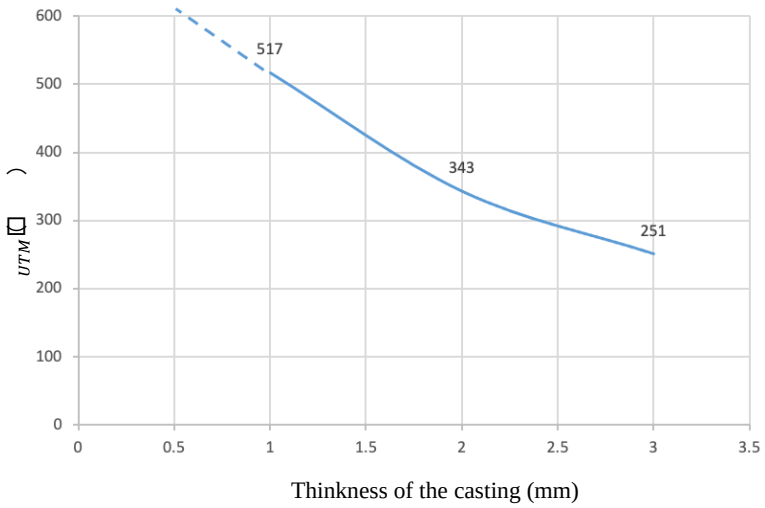

Figure 8. Tensile strength of the casting with different thicknesses.

Figure 6 shows the analysis of X-ray diffraction results of Al–Mn–Ce alloy at different cooling rates. It can be seen from Figure 6 that when $Al_{92}Mn_6Ce_2$ alloy is prepared using the

cast-in metal mold method with casting bar thicknesses of 1 and 0.5 mm, the main formation phases in the alloy are the Al_6Mn phase and face-centered cubic aluminium phase.

The tensile strength of the casting with different thicknesses is shown in Figure 8. Since the 0.5 mm thick samples have a small traction for tensile samples, data were not available, the strength of the casting with 1 mm thickness is 517 MPa.

4. CONCLUSIONS

In the paper, by numerical simulation (ABAQUS, FEM) and experimental methods, the cooling rate was investigated by changing the product thickness (0.3, 0.5, 1, 2, 3 and 20 mm) to fabricate Al-based two-phase nanostructured materials casted through a copper mold. The simulation and experimental results show that the solidificated intermetallic phases have a decreasing size corresponding to the increasing cooling rate.

The effect of cooling speed with different thicknesses of 20, 3, 1 and 0.5 mm corresponds to increasing cooling rates of 10^2, 10^3 and 10^4 K/s, respectively. It can be easily observed that the secreted intermetallic phases have a decreasing size: when the cooling speed is 10^2 *K/s*, the intermetallic phase has a rather large size (10 - 20 μm) due to its long contact time with liquid metal and favorable conditions for growth.

The strength of 1 mm thick casting is 517 MPa.

Acknowledgements. The authors are grateful for the support from the B2022-BKA-16 project funded by the Ministry of Education and Training of Viet Nam.

CRediT authorship contribution statement. Nguyen Hong Hai: Supervision, Methodology, Investigation, Funding acquisition, Review and Editing. Le Minh Duc: Formal analysis, Data curation, Investigation. Hoang Thi Ngoc Quyen: Formal analysis, Investigation. Pham Quang: Writing - Original Draft, Data analysis, Methodology, Review and Editing.

Declaration of competing interest. The authors declare that they have no known competing financial interests or personal relationships that could have appeared to influence the work reported in this paper.

REFERENCES

1. Shin S., Yeom G., Kwak T., Park I. - Microstructureandmechanicalpropertiesof TiB-containing Al-Zn binary alloys, J. Mater. Sci. Technol. **32** (2016) 653-659. DOI: 10.1016/j.jmst.2016.04.016.
2. Shin S., Lim K., Park I. - Characteristics and microstructure of newly designed Al-Zn-based alloys for the die-casting process, J. Alloy. Comp. **671** (2016) 517-526.https://doi.org/10.1016/j.jallcom.2016.02.127.
3. Guo H., Yang X., Wang J., Hu B., Zhu G. - Effects of rheoforming on micro structures and mechanical properties of 7075 wrought aluminium alloy, T. Nonferr. Metal Soc. **20** (2010) 355-360.https://doi.org/10.1016/S1003-6326(09)60146-1.
4. Duc D. M., Hai N. H., and Quang P. - Modeling of continuous rheo-casting the A356 alloy by finite element method (FEM), Sci. Tech. Metals **46**, 37 (2013).
5. Tai N. T., Duc D. M., Hai N. H., and Quang P. - Optimization of flow behavior in high-pressure die casting by the Pro/Engineer virtualmanufacturing, J. of Science and Technology **5A** (201) (2013).

6. Tai N. T., Duc D. M., Hai N. H., and Quang P. - Effect of pressure on microstructure and mechanical properties of A356 aluminium alloy during rheo-diecasting process (RDC), J. of Science and Technology **5A** (194) (2013).
7. Duc D. M., Hai N. H., and Quang P. - Simulation and experimental study on the steady conduction solution for continuous rheo-casting for A356 alloy, Korean J. Met. Mater. **55** (3) (2017), 202-208.https://doi.org/10.3365/KJMM.2017.55.3.202
8. Nguyen Hong Hai, Pham Quang - Effect of Pressure on Solidification Process and Mechanical Properties During Semi-Solid Casting by Computational Fluid Dynamics (CFD). Advances in Materials. **7** (2)(2018) 44-49. doi: 10.11648/j.am.20180702.15.
9. Górny M., Tyrała E. - Effect of Cooling Rate on Microstructure and Mechanical Properties of Thin-Walled Ductile Iron Castings. J. of Materi Eng and Perform.**22** (2013) 300–305.https://doi.org/10.1007/s11665-012-0233-0.
10. Tang H. P. *et al.* - Effect of cooling rate on microstructure and mechanical properties of an Al-5.0Mg-3.0Zn-1.0Cu cast alloy, Journal of Alloys and Compounds, **801** (2019) 596-608.https://doi.org/10.1016/j.jallcom.2019.06.002.
11. Juan W. *et al.* - Effect of cooling rate on the microstructure and thermal expansion properties of Al–Mn–Fe alloy, Reviews on Advanced Materials Science. **61** (2022) 265–275.https://doi.org/10.1515/rams-2022-0031.
12. Zare M.A., Taghiabadi R. & Ghoncheh M.H. - Effect of Cooling Rate on Microstructure and Mechanical Properties of AA5056 Al-Mg Alloy. Inter Metalcast.**16** (2022) 1533–1543.https://doi.org/10.1007/s40962-021-00704-6.
13. Tsai A. P., Inoue A., and Masumoto T. - A stable quasicrystal in Al–Cu–Fe System. Japanese Journal of Applied Physics. **26** (9A)(1987), id. L1505.
14. Yadav T. P. and Mukhopadhyay N. K. - Quasicrystal: A low-frictional novel material. Chemical Engineering. **19** (2018) 163-169.https://doi.org/10.1016/j.coche.2018.03.005.
15. Galano M., Audebert F., Escorial A. G., Stone I. C., and Cantor B. - Nanoquasicrystalline Al–Fe–Cr-based alloys with high strength at elevated temperature. Journal of Alloys and Compounds. **495** (2) (2010) 372-376.https://doi.org/10.1016/j.jallcom.2009.10.208.
16. Zupanič F., Bončina T., Križman A., Grogger W., Gspan C., Markoli B., *et al.* - Quasicrystalline phase in melt-spun Al–Mn–Be ribbons. Journal of Alloys & Compounds. **452** (2) (2008) 343-347.https://doi.org/10.1016/j.jallcom.2006.11.041.
17. Inoue A., Watanabe M., Kimura H. M., Takahashi F., Nagata A., and Masumoto T. - High mechanical strength of quasicrystalline phase surrounded by fcc-Al phase in rapidly solidified Al–Mn–Ce alloys. Materials Transactions, JIM. **33** (1992) 723-729. https://doi.org/10.2320/matertrans1989.33.723.
18. Chang H. J., Fleury E., Song G. S., Lee M. H., Kim W. T., and Kim D. H. - Microstructure modification and quasicrystalline phase formation in Al–Mn–Si–Be cast alloys, Materials Science & Engineering A. **375** (377) (2004) 992 -997. https://doi.org/10.1016/j.msea.2003.10.004.
19. Chang H. J., Fleury E., Song G. S., Kim W. T., and Kim D. H. - Formation of quasicrystalline phases in Al-rich Al–Mn–Be alloys, Journal of Non-Crystalline Solids **334** (2004) 12-16. https://doi.org/10.1016/j.jnoncrysol.2003.11.005.
20. Zupanic F., Boncina T., Rozman N., Anzel I., Grogger W., Gspan C., *et al.* - Development of an Al–Mn–Be–Cu alloy with improved quasicrystalline forming ability, International

Journal for Structural Physical & Chemical Aspects of Crystalline Materials **223** (11–12)(2008) 735-738.https://doi.org/10.1524/zkri.2008.1037.

21. Eisenbud M., Kotin P., and Miller F. - Is beryllium carcinogenic in humans? Journal of Occupational & Environmental Medicine. **39** (3)(1997) 205-208.
22. Schurack F., Eckert J., and Schultz L. - Synthesis and mechanical properties of cast quasicrystal-reinforced Al- alloys. Acta Materialia **49** (8)(2001) 1351-1361. https://doi.org/10.1016/S1359-6454(01)00045-3.
23. Coury F. G., Botta W. J., Bolfarini C., KiminamiC. S. and Kaufman M. J. - Reassessment of the effects of Ce on quasicrystal formation and microstructural evolution in rapidly solidified Al–Mn alloys. Acta Materialia. **98** (2015) 221-228. https://doi.org/10.1016/ j.actamat.2015.07.046.
24. Stan K., Lityńska-Dobrzyńska. L., Dutkiewicz J., Rogal L., and Janus A. M. - TEM study of quasicrystals in Al–Mn–Fe melt-spun ribbon. Solid State Phenomena. **186**(2012) 255–258.DOI:10.4028/www.scientific.net/SSP.186.255.
25. Stan K., Lityńska-Dobrzyńska L., Lábár J.L., and Góral A. - Effect of Mo on stability of quasicrystalline phase in Al–Mn–Fe alloy. Journal of Alloys and Compounds. **586** (2014) 395–399.https://doi.org/10.1016/j.jallcom.2012.12.013.
26. Stan-Głowińska K., Lityńska-Dobrzyńska L., Kania B., Dutkiewicz J., Skuza W., Wojewoda-Budka J., *et al*. - Effects of hot-compaction on the structure and properties of AlMn-Fe-X alloys strengthened with quasi-crystalline icosahedral phase, Materials & Design. **126** (2017) 162-173. https://doi.org/10.1016/j.matdes.2017.04.043.
27. Stan-Głowińska K. and Lityńska-Dobrzyńska L. - Influence of Fe addition on the formation of a quasicrystalline phase in bulk Al-rich Al-Mn base alloys. Materials Characterization **128** (2017) 203-208.https://doi.org/10.1016/j.matchar.2017.04.006.
28. Balanetskyy S., Pavlyuchkov D., Velikanova T., and Grushko B., The Al-rich region of the Al-Fe-Mn alloy system, Journal of Alloys and Compounds **619** (2014) 211-220. https://doi.org/10.1016/j.jallcom.2014.08.232.
29. Abaqus/CAE User's Guide: Abaqus 6.14, © Dassault Systèmes, 2011.
30. Abaqus/Theory Manual: Uncoupled heat transfer analysis, © Dassault Systèmes, 2011.
31. Brandes E. A. - Smithells Metals Reference Book (Seventh Edition) Published by Butterworth & Co. Ltd, 1983.